Int J Earth Sci (Geol Rundsch) (2016) 105:1453–1465
DOI 10.1007/s00531-015-1264-1

ORIGINAL PAPER

Linking SO_2 emission rates and seismicity by continuous wavelet transform: implications for volcanic surveillance at San Cristóbal volcano, Nicaragua

Vladimir Conde[1] · Stefan Bredemeyer[2] · J. Armando Saballos[3] · Bo Galle[1] · Thor H. Hansteen[4]

Received: 23 April 2015 / Accepted: 14 October 2015 / Published online: 3 November 2015

Abstract San Cristóbal volcano is the highest and one of the most active volcanoes in Nicaragua. Its persistently high activity during the past decade is characterized by strong degassing and almost annual VEI 1–2 explosions, which present a threat to the local communities. Following an eruption on 8 September 2012, the intervals between eruptions decreased significantly, which we interpret as the start of a new eruptive phase. We present here the results of semi-continuous SO_2 flux measurements covering a period of 18 months, obtained by two scanning UV-DOAS instruments installed as a part of the network for observation of volcanic and atmospheric change project, and the results of real-time seismic amplitude measurements (RSAM) data. Our data comprise a series of small to moderately explosive events in December 2012, June 2013 and February 2014, which were accompanied by increased gas emissions and seismicity. In order to approach an early warning strategy, we present a statistical method for the joint analysis of gas flux and seismic data, by using continuous wavelet transform and cross-wavelet transform (XWT) methods. This analysis shows that the XWT coefficients of SO_2 flux and RSAM are in good agreement with the occurrence of eruptive events and thus may be used to indicate magma ascent into the volcano edifice. Such multi-parameter surveillance efforts can be useful for the interpretation and surveillance of possible eruptive events and could thus be used by local institutions for the prediction of upcoming volcanic unrest.

Keywords DOAS · Volcanic SO_2 · RSAM · Wavelets · CWT and XWT

✉ Vladimir Conde
conde@chalmers.se

Stefan Bredemeyer
sbredemeyer@geomar.de

J. Armando Saballos
armando.saballos@gf.ineter.gob.ni

Bo Galle
bo.galle@chalmers.se

Thor H. Hansteen
thansteen@geomar.de

[1] Department of Earth and Space Sciences, Chalmers University of Technology, Hörsalsvägen 11, 412 96 Gothenburg, Sweden

[2] SFB 574 and GEOMAR Helmholtz Centre for Ocean Research Kiel, Wischhofstr. 1-3, 24118 Kiel, Germany

[3] Instituto Nicaragüense de Estudios Territoriales (INETER), Apdo., 2110 Managua, Nicaragua

[4] GEOMAR Helmholtz Centre for Ocean Research Kiel, Wischhofstr. 1-3, 24118 Kiel, Germany

Introduction

Surveillance of volcanoes is fundamental for hazard assessment and mitigation prior to and during periods of volcanic crisis. During the last decades, significant progress has been achieved on this issue through the deployment of a diversity of multi-parameter surveillance methods. Seismicity is still considered one of the most reliable parameters for monitoring volcanic activity; hence, it is probably the most popular monitoring tool used by volcanologists (e.g. Tilling 2008; D'Alessandro et al. 2013). Volcanic gas emissions also play an important role in volcanic surveillance (e.g. Casadevall et al. 1983; Symonds et al. 1994; Burton et al. 2007) since eruptions are often heralded by increases in volcanic SO_2 emissions, which originate from the ascent of fresh magma to shallower crustal levels (e.g. Daag et al. 1996).

Measuring sulphur dioxide (SO_2) emissions has been successfully achieved using ground-based remote sensing techniques such as the correlation spectrometer (COSPEC; Hoff and Millan 1981), differential optical absorption spectroscopy (DOAS; Platt and Stutz 2008) and more recently SO_2 cameras (Mori and Burton 2006; Bluth et al. 2007). Mobile and scanning DOAS are among the most commonly used approaches for volcanic gas measurements (Galle et al. 2002; Edmonds et al. 2003; Platt and Stutz 2008; Burton et al. 2009; Boichu et al. 2010; Galle et al. 2010). The network for observation of volcanic and atmospheric changes (NOVAC) project is monitoring SO_2 emissions of about 20 volcanoes around the world using scanning DOAS instruments (NOVAC instruments; Galle et al. 2010). This instrumental set-up has produced a wealth of semi-continuous SO_2 flux measurements and thus allows for near-real-time side-to side evaluation of SO_2 emissions with other data set, e.g. with seismic signals. The potential of combining seismic and SO_2 measurements as a surveillance tool has been demonstrated for different scenarios (e.g. Petersen et al. 2006; Olmos et al. 2007; Nadeau et al. 2011; Conde et al. 2013; Waite et al. 2013; Hidalgo et al. 2015). The recently enhanced activity at San Cristóbal provides a suitable case study for conducting a joint analysis of seismic and gas measurements by using cross-wavelet transform (XWT), which is a technique aimed to locate the temporal occurrence of significant spikes and oscillations that may help to ascertain the underlying processes leading to eruptive events.

Background

San Cristóbal volcano is a 1745-m-high basaltic-to-andesite stratovolcano located in north western Nicaragua approximately 15 km north-east of the city of Chinandega (12.70°N 87.0°W; Fig. 1). Volcanic activity at San Cristóbal is characterized by a persistently strong open-vent and fumarolic degassing, as stated by previous studies summarized in Table 1 (Mather et al. 2006; Barrancos et al. 2008; Rivera et al. 2009; Fischer von Mollard 2013). San Cristóbal volcano exhibits cyclical transitions between periods of quiescent degassing and substantial increases in gas emissions during the onset of eruptive events that are mostly characterized by minor-to-moderate explosions accompanied by ash fallout. These transitions have occurred at a higher rate during the last 2 years with VEI 1–VEI 2 eruptive events occurring approximately twice a year (Smithsonian-Institution 2014).

Methodology

SO_2 flux measurements

SO_2 flux measurements were made by two NOVAC instruments installed on the west flank of San Cristóbal volcano (Fig. 1). The instrument acquires UV-scattered sunlight spectra by scanning along a vertical plane spanning 180°

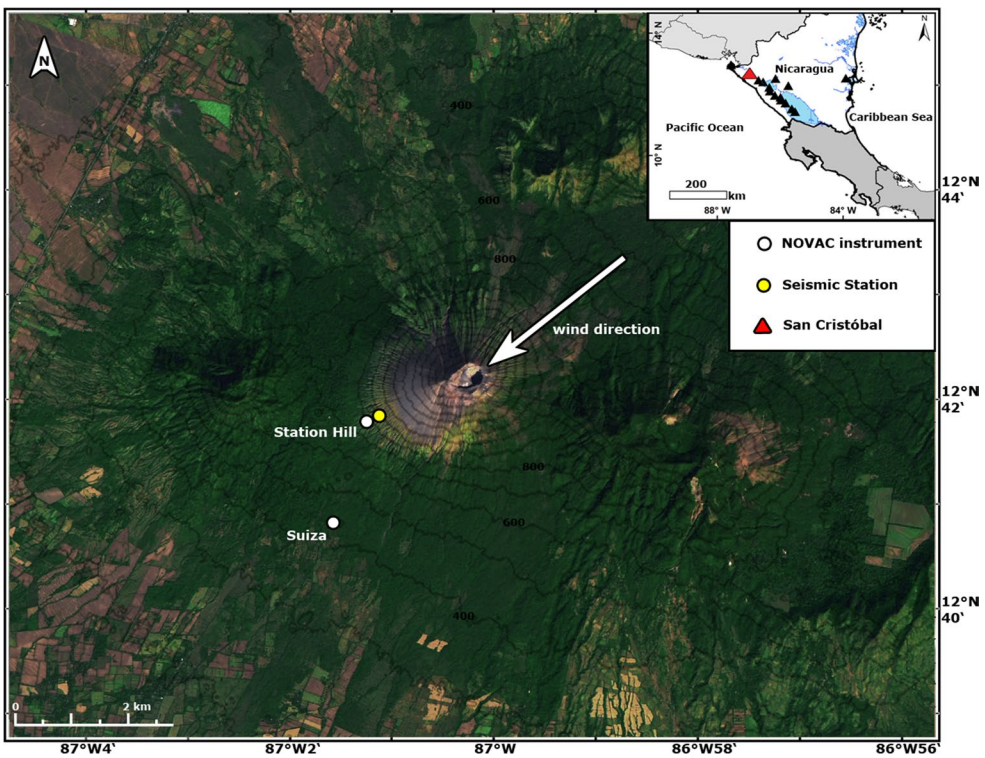

Fig. 1 Map showing the location of the NOVAC instruments and the seismic station on the south-western flank of San Cristóbal volcano. The map is based on a composite of spectral bands from Landsat eight scene LC80170512014016LGN00 (16 January 2014) available from the US Geological Survey (https://lta.cr.usgs.gov/L8). *Inset* map of the volcanic arc in Nicaragua (*black triangles*)

Table 1 Compilation of previous SO_2 emission measurements at San Cristóbal volcano

Date	SO_2 flux (t day^{-1})	References
November 2003	800 ± 190	Mather et al. (2006)
March 2006	317 ± 274	Barrancos et al. (2008)
November 2006	1406 ± 805	Rivera (2009)
2007	515 ± 517	Fischer von Mollard (2013)
2008	244 ± 203	Fischer von Mollard (2013)
2009	1515 ± 891	Fischer von Mollard (2013)
2010	893 ± 727	Fischer von Mollard (2013)
2011	627 ± 235	Fischer von Mollard (2013)
2012	1489 ± 671	Fischer von Mollard (2013)

from one horizon to the other in angular steps of 3.6°. The principal component is a spectrometer (Ocean Optics®, S2000), which operates in the wavelength range 280–425 nm divided into 2048 channels yielding a spectral resolution of approximately 0.6 nm. The instrument runs during daylight hours, and the signal-to-noise ratio is improved by adding 15 spectra and adjusting automatically the exposure time in order to avoid light saturation in the spectrometer detector.

The SO_2 column amount was retrieved from the spectra for each angular step, applying DOAS in the wavelength region of 310–322 nm (Platt and Stutz 2008), where the SO_2 absorption cross section still has a pronounced signature and low sensitivity to scattering and straylight (Johansson 2009; Galle et al. 2010). More advanced details about the NOVAC instruments and column retrievals are described in Galle et al. (2010) and Edmonds et al. (2003).

In order to determine the SO_2 flux, geometric information of the plume is required in addition to the gas columns as shown in Eq. (1) from Hoff and Millan (1981).

$$\text{Flux} = W_s \times |\cos(W_d - \text{compass})| \times P_H \times \sum_{i=0}^{N-1} |\tan\alpha_{i+1} - \tan\alpha_i| \times \text{VCD}_i \quad (1)$$

where VCD_i is the SO_2 vertical columns density estimated at the angular step α_i, which corresponds to the angle between the column and the zenith. W_s and W_d are the wind speed and plume direction at the plume height (P_H), and *compass* is the direction perpendicular to the plane of scanning. The plume at San Cristóbal volcano usually bends over shortly after leaving the crater; thus, P_H was assumed to be the same as the crater height (1745 m.a.s.l.), while the plume direction was geometrically calculated by combining plume height and the scanning angles α which show the strongest absorption. The plume (wind) speed was obtained from the weather forecast model GFS provided by the National Ocean and Atmospheric Administration (NOAA), which has a grid length of 1° and a time resolution of 3 h.

The uncertainty of the flux measurements using DOAS results from a combination of various error sources including spectroscopy, local weather conditions and inaccuracies in the estimation of the plume geometry. Previous studies have provided a statistical approach in order to quantify the measurement error, whereas the modelled wind speed has been identified as the predominant error source accounting for an uncertainty of 20–30 % (e.g. Mather et al. 2006; Rivera et al. 2009; Galle et al. 2010).

Considering the proximity of the instruments to the emission source and the very well-defined plume signatures in most of the scans, the estimated total measurement error at San Cristóbal volcano is assumed to be 35 % under optimal weather conditions. The sampling period is not uniform since the exposure time is automatically adjusted depending on the visibility conditions; thus, under clear sky conditions it is possible to acquire up to 60 measurements per day. However, having an uneven sampling rate prevents the application of the data analysis methods which will be further discussed in the following sections. Due to the limitations imposed by the uneven sampling rate and the impossibility of perform measurements during nighttime, our SO_2 flux time series is portrayed as the daily average of the gas emissions and its respective daily standard deviation.

SO_2 flux pre-processing

The daily average of the SO_2 flux can be a good approximation of the flux evolution through time, while the variability of the standard deviation is caused by a combination of several parameters including transient eruptivity events, the random nature of the degassing processes and atmospheric perturbations. In order to obtain a better estimation of the underlying long-term SO_2 emissions, a common mathematical approach is to smooth the time series using the Kalman filter (Kalman 1960), which has been successfully applied for data estimation of geophysical measurements (e.g. Anderson 2001; Evensen 2003; Nagarajan et al. 2012; Yan et al. 2014). In contrast to traditional filtering techniques, which are based on the removal of "undesired components", the Kalman filter assumes a state-space (time) model estimator and explicitly accounts for measurement and modelling error as described by the following equations:

$$X_n = X_{n-1} + W_n \quad (2a)$$

$$W_n \sim N(0, Q_n) \quad (2b)$$

$$Y_n = X_n + V_n \quad (3a)$$

$$V_n \sim N(0, R_n) \tag{3b}$$

Equation (2) corresponds to the current estimate of the time-dependent process X_n, which in this case corresponds to the daily flux. The estimate of X_n is based on the previous estimate X_{n-1} and the expected variability W_n with a variance of Q_n. This estimator is termed the random walk model (RWM), which despite its simplicity has been demonstrated to be a good estimator in other atmospheric measurements scenarios (Mulquiney et al. 1995). Similarly, Eq. (3) models the estimate of X_n and its respective measurement error V_n with a variance of R_n.

The Kalman filter is implemented by means of a recursive sequence of two steps: estimation and correction. In accordance with the RWM, the estimation step is described by Eq. (4) as follows:

$$\hat{X}_n^- = \hat{X}_{n-1} \tag{4a}$$

$$\hat{P}_n^- = \hat{P}_{n-1} + Q_{n-1} \tag{4b}$$

where $\hat{X}_n^-$ and $\hat{P}_n^-$ correspond to model-estimated flux and variance, respectively. The most difficult aspect of assuming a RWM is a realistic estimate of the expected variability W_n. However, we have considered a statistical approach, as illustrated in Myers and Tapley (1976), where the flux variance Q_n during a period of 1 day can be assumed to be a suitable approximation of the expected variability.

The correction step, described by Eq. (5), links the previously estimated parameters with the actual flux measurements Y_n based on the measurement model previously described in Eq. (3).

$$K_n = \frac{\hat{P}_n^-}{\hat{P}_n^- + R_n} \tag{5a}$$

$$\hat{X}_n = \hat{X}_n^- + K_n\left(Y_n - \hat{X}_n^-\right) \tag{5b}$$

$$\hat{P}_n = (1 - K_n)\hat{P}_n^- \tag{5c}$$

where K_n corresponds to the so-called Kalman gain (Welch and Bishop 1995) and the error variance R_n is akin to the previously estimated flux measurement error of 35 %. $\hat{X}_n$ and $\hat{P}_n$ are the updated–estimated flux and variance, respectively, which correspond to the Kalman "filtered" values and the initial parameters for the next iteration (Eq. 4). For simplicity, the initial conditions of the algorithm are $\hat{X}_0 = Y_0$ and $\hat{P}_0 = 0$. A comparison of the Kalman estimated SO_2 flux versus the individual daily SO_2 flux measurement during a selected period of 4 months at San Cristóbal volcano is displayed in Fig. 2 where it is shown that smoothing the time series by means of a Kalman filter provides a balanced trade-off between the signal trend and its natural variability. A more general description of the recursive estimator–corrector Kalman Filter algorithm can be found elsewhere (e.g. Myers and Tapley 1976; Mulquiney et al. 1995; Welch and Bishop 1995).

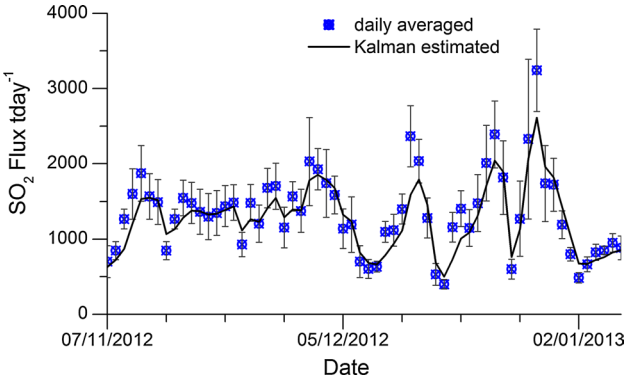

Fig. 2 Comparison between daily average SO_2 fluxes and the Kalman estimated fluxes from November 2012 to January 2013

Seismic data

Real-time seismic amplitude measurements (RSAM; Endo and Murray 1991) were calculated from measurements of the three-component broadband station CRIN that belongs to the seismic network of Instituto Nicaragüense de Estudios Territoriales (INETER) and is located on the southwestern flank of the volcano (Fig. 1). Each individual RSAM measurement corresponds to the average value of the seismic amplitude during 10 min; however, the averaging time was increased up to 1 day in order to make it coherent with the daily sampling rate of the SO_2 flux. The RSAM time series was pre-processed using a Kalman filter algorithm with the same approach as the one described in the previous section.

Wavelet analysis

Several methods can be applied in order to perform a joint analysis of volcanic SO_2 fluxes and RSAM. Some classical approaches such as cross-correlations and Fourier transform may produce acceptable results when considering time series with short-time windows and some degree of stationarity. However, through extended periods of analysis, the underlying volcanic processes exhibit transient changes, which are associated with variations in the eruptive regime and are reflected in discontinuities of the spectral characteristics of the both SO_2 fluxes and RSAM time series. Continuous wavelet transform (CWT) is a mathematical tool that achieves to resolve both stationary and transient changes in a signal. It decomposes a time series into time–frequency components allowing time localization

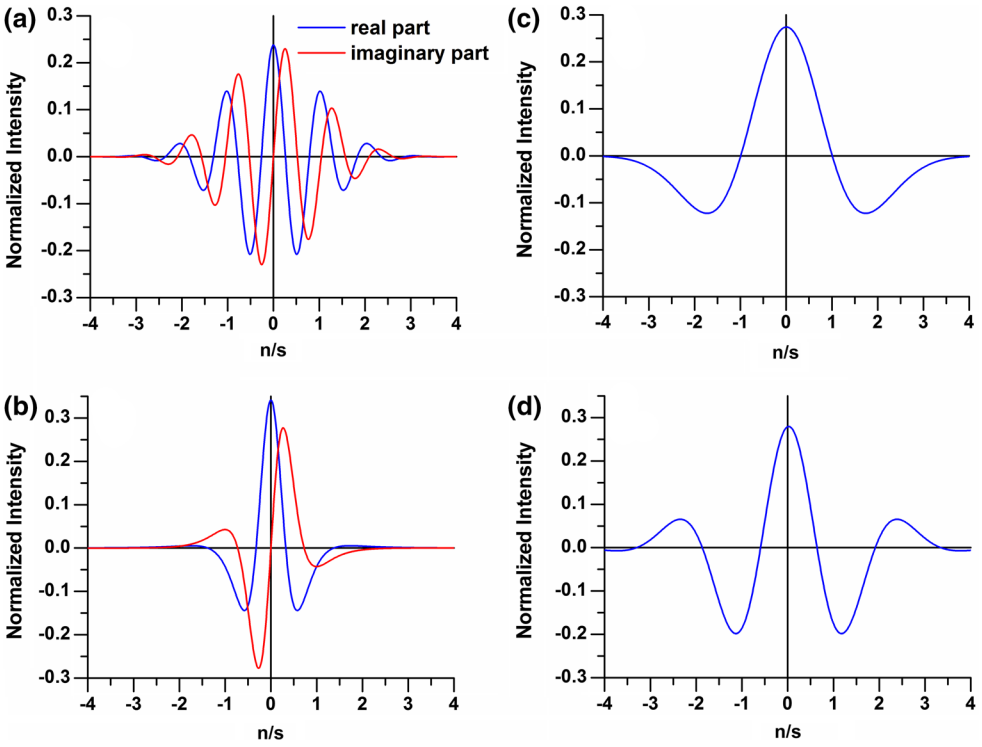

Fig. 3 Normalised mother wavelets $\psi(n/s)$ used in this paper. The *plots* on the *left side* of the picture correspond to complex wavelets, while the *plots* on the *right side* correspond to real wavelets. **a** Morlet, **b** Paul. DOG of *m*th order: **c** DOG ($m = 2$), **d** DOG ($m = 6$)

of spectral characteristics that are statistically significant during a particular period. Due to the non-stationary nature of many geophysical and atmospheric systems, several studies have applied this time-series analysis technique, e.g. in climatology and astrophysics (e.g. Kestin et al. 1998; Torrence and Webster 1999; De Moortel et al. 2000; Mwale and Gan 2005; Wang and Gao 2013).

In simplified words, a wavelet $\psi(n/s)$ is a finite energy function that resembles a short oscillation, which can be time translated and scale compressed or expanded. The mathematical basis and details concerning the choice and design of wavelet functions are out of the scope of this article and can be found elsewhere (e.g. Daubechies 1990; Weng and Lau 1994; Lau and Weng 1995); however, out of several possible wavelet functions, this article examines the performance of four popular wavelets: the complex wavelets Morlet and Paul and the real wavelets derivative of Gaussian (DOG) of *m*-th order DOG ($m = 2$) and DOG ($m = 6$) as shown in Fig. 3.

The CWT $W_n(s)$ can be defined as the convolution of the time series X_n with a scaled wavelet function $\psi(n/s)$.

$$W_n(s) = \sum_{n'=0}^{N-1} X_t \psi \left[\frac{n' - n}{s} \delta t \right] \tag{6}$$

where δ_t is the sampling period and s is the CWT scale (period). The spectral decomposition is achieved by discretely compressing and/or expanding the scale s prior to performing the convolution. One of the most important criteria concerning the choice of wavelet is the trade-off between time and frequency resolution. In this regard, the Morlet wavelet is highly popular in geophysical applications due to its well-balanced proportion between these two parameters (Torrence and Compo 1998). However, for applications that aim at an enhanced period–frequency resolution the Paul wavelet may be a better choice. The outcome of $W_n(s)$ is an array of coefficients distributed according to their corresponding timescale, normally displayed as a contour or temperature map where the amplitudes of the wavelet coefficients (W_n) are plotted at their respective period (or frequency) and time. Figure 4 shows a comparison between the CWT for SO_2 flux measurements at San Cristóbal volcano during a period of 4 months using Morlet and Paul wavelets.

The statistical significance of the coefficient amplitudes was calculated, assuming that their spectral properties depict increased amplitude at lower frequencies. This spectral feature that is commonly observed in geophysical time series is normally referred as red noise and can be modelled by a stochastic first-order autoregressive (AR1) process (Allen and Smith 1996). A typical assumption is to consider that the statistical significance of wavelets coefficients is 5 % (95 % confidence level) against red noise (Grinsted et al. 2004).

The XWT is just an extension of the CWT for performing a joint analysis of two time series by the conjugate product (*) of their CWT, as shown in Eq. (7).

$$W_n(s)^{xy} = W_n(s)^x W_n(s)^{y*} \tag{7}$$

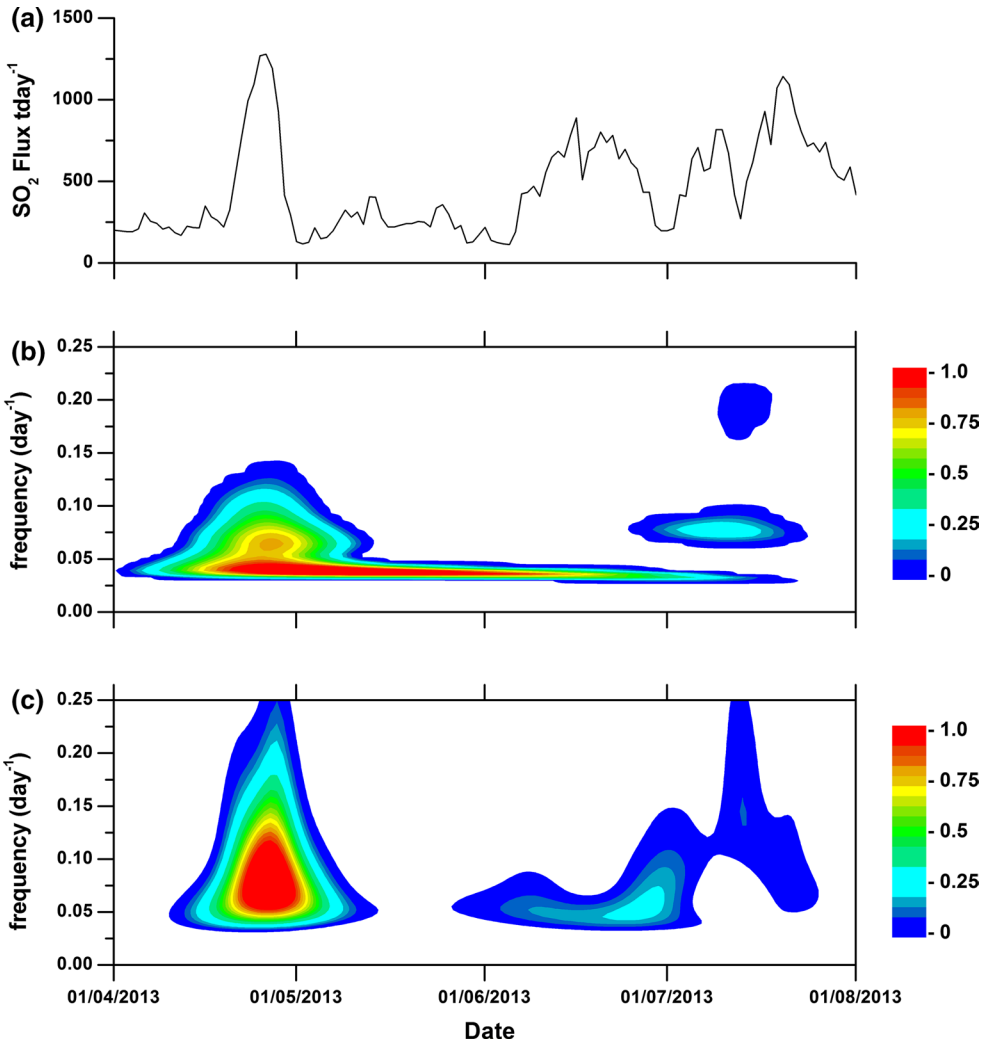

Fig. 4 Comparison between the wavelets Morlet and Paul for SO_2 fluxes at San Cristóbal during the period April–August 2013. **a** SO_2 fluxes. **b** Contour map of SO_2 CWT power spectrum coefficients using a Morlet Wavelet. **c** Contour map of SO_2 CWT power spectrum coefficients using a Paul Wavelet. The *coloured* contours correspond to the wavelet coefficients with greater than 95 % significant difference from *red* noise

Unlike traditional correlation methods, XWT allows to correlate common spectral–amplitude signatures of a pair of signals at localized periods, and thus, it can be used to detect transient association between both signals. Further details of the implementation of the CWT, XWT and the 5 % statistical significance can be found in Torrence and Compo (1998) and Grinsted et al. (2004), respectively.

Results

Chronology of SO_2 degassing and seismicity

Figure 5 shows a comparison between SO_2 fluxes and RSAM, outlining three periods of enhanced volcanic activity characterized by small-to-moderate explosions, ash emissions and strong degassing. The first period started during the first week of November 2012, when seismicity sharply increased by a factor of 2 and SO_2 emissions even quadrupled from a background of 250 t day^{-1} measured during the second half of October, to approximately 1000 t day^{-1} in mid-November. Gas emissions featured pulsating patterns which continually increased through mid-December and culminated in a peak value of approximately 2500 t day^{-1} on December 26, only 1 day after the eruption started. About 3 weeks before the onset of the eruption (December 25), the co-variation between RSAM and degassing trends started to increase, gaining correlation towards the explosive events. Approximately 1 week after the crisis started, there were no more reports of explosive activity and SO_2 emissions gradually decreased, which was additionally reflected by a decrease in the pulsating patterns and a decrease in correlation between the two signals. By the middle of February through mid-April 2013, the SO_2 emissions remained relatively stable, reaching an average flux of ≈250 t day^{-1}. Unfortunately RSAM could not be calculated for the period 28 December 2012 to 01 March 2013, since the seismic station did not work properly as a result of ash depositions from the eruptions. Seismograms provided by INETER, however, clearly show that

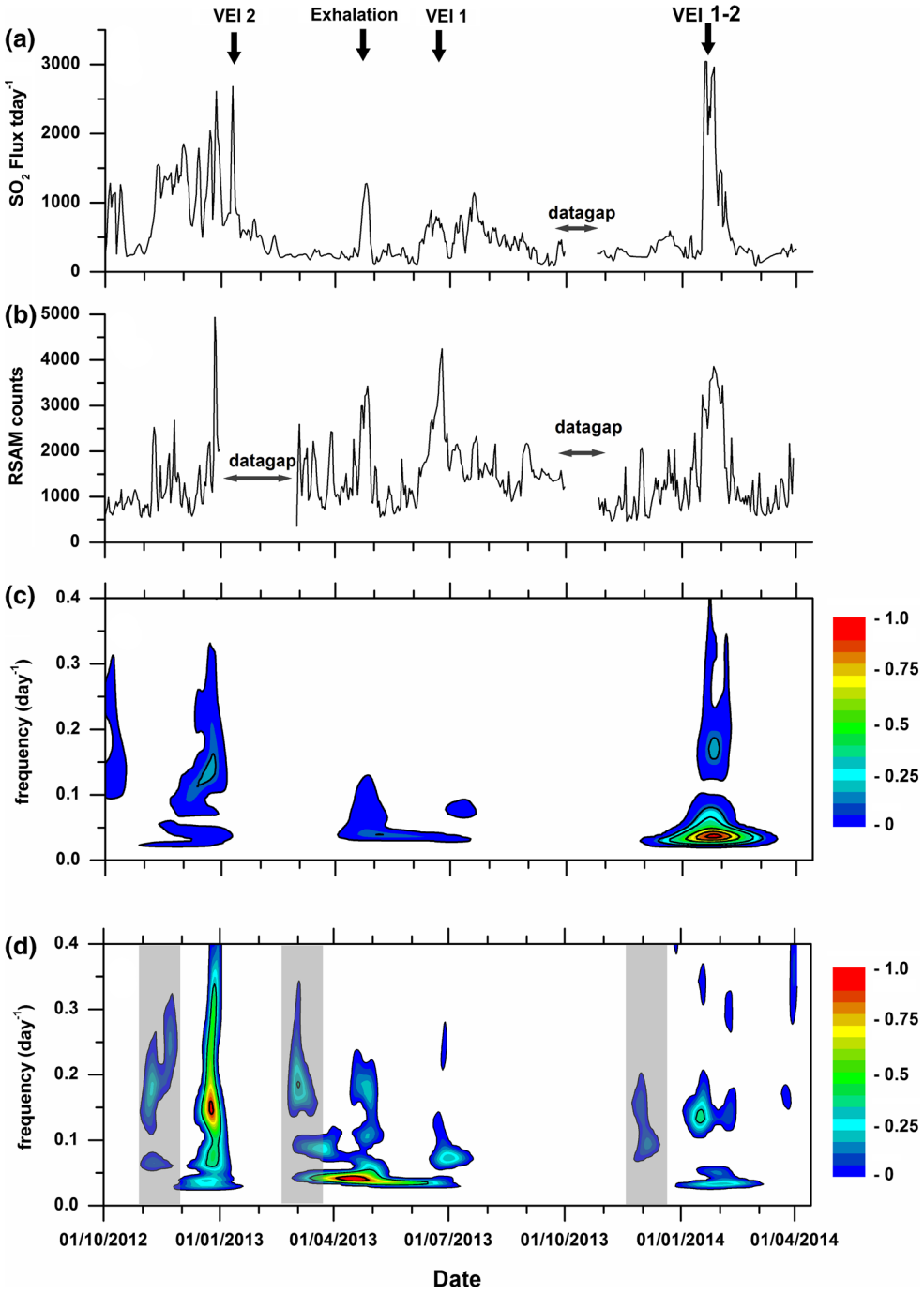

Fig. 5 Estimated fluxes and RSAM with their respective wavelet transform at San Cristóbal during the period: October 2012–April 2014. **a** SO_2 fluxes. **b** RSAM counts. **c** Contour map of SO_2 CWT power spectrum coefficients. **d** Contour map of RSAM CWT power spectrum coefficients with precursory periods highlighted by the *grey insets*. The CWT power spectrum coefficients were obtained by using the Morlet wavelet. The *coloured* contours correspond to the wavelet coefficients with greater than 95 % significant difference from *red* noise. The *arrows mark* periods of enhanced eruptive activity and amplitude estimates of explosions are indicated by the volcanic explosivity index (VEI)

post-eruptive seismicity gradually decreased with some recurrent short episodes of banded tremor (http://www.volcanodiscovery.com/san-cristobal/news/2013/all.html).

Volcanic activity increased during the second half of April 2013 and climaxed in a relatively abrupt gas exhalation event end of April 2013 (April 21–29), which was clearly correlated with an increase in RSAM counts by a factor 3, and the SO_2 flux raised from 250 to approximately 800 t day^{-1} through a period of about 10 days before returning to its initial value. Following this precursory event, gas emissions diminished to about 100 t day^{-1} and were well below background shortly before a series of VEI 1 explosive events occurred during the period 7–11 June 2013, accompanied by ash emissions. Seismicity and gas emissions gradually increased after the explosions. Despite the intensity of the explosions, SO_2 emissions, however, increased only slightly to values around 500 t day^{-1}, while in contrast, RSAM increased significantly by a factor 4. Afterwards, SO_2 emissions and RSAM gradually returned to their pre-eruptive background values.

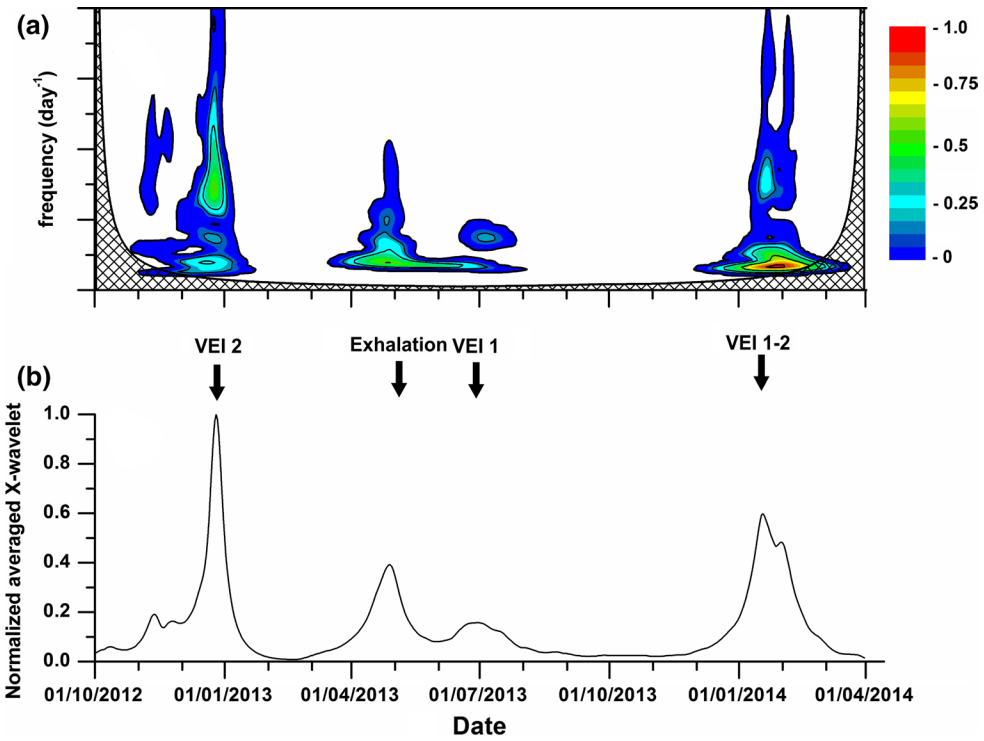

Fig. 6 **a** Contour map of XWT power spectrum coefficients between the SO_2 fluxes and RSAM (Fig. 5a, b). The *coloured* contours correspond to the cross-wavelet coefficients with greater than 95 % significant difference from *red* noise. The *area filled* with *black crosses* and *outlined* in *black* indicates the COI, where edge effects become important, **b** XWT scale-averaged coefficients. The *arrows mark* the *onset* of periods of enhanced eruptive activity which are shown in Fig. 5. The discontinuities correspond to measurement gaps

Following approximately 6 months of relative calm, volcanic activity resumed again during the period 17 January to 4 February 2014. A threefold increase in RSAM correlated well with a series of 12 gas exhalation events on January 17 followed by VEI 1–2 explosive events on 4 February 2014 and a sustained increase in the SO_2 emissions which reached a peak value of approximately 3000 t day^{-1} during the explosive events.

XWT joint analysis

During time windows close to and including the main eruptive events, the Morlet CWTs of both time series show clear patterns of statistically significant coefficients and frequency shifts from a background periodicity of 0.1–0.35 day^{-1} (10–2.8 days) (Fig. 5c, d). Hence, the correlation between both times series was investigated in view of their common spectral–amplitude signatures by applying XWT, and the resultant coefficients are shown in Fig. 6a. In comparison with the individual CWT of both SO_2 fluxes and RSAM, the patterns of the statistically significant coefficients of the XWT exclusively show the features, which both time series have in common and reveal a pronounced signature. These are explicitly restricted to periods with immediate temporal proximity to evident eruptive activity. A better representation of the temporal variation is obtained by averaging the statistically significant XWT coefficients amidst their predominant periodical range (0.03–0.4 day^{-1} or 33.3–2.5 days). Figure 6b shows the result of the averaged XWT coefficients, and the main eruptive events are in good agreement with the averaged coefficient peaks.

Discussion

The SO_2 time series indicate that persistent degassing of San Cristóbal averaged approximately 1000 t day^{-1} during the period reported in this study, while in the immediate temporal proximity of eruptive events, significant increases in the SO_2 emissions and seismicity are observed in their time series and the patterns of the corresponding CWT coefficients. A closer look at the grey insets of Fig. 5d indicates that periods of high RSAM CWT coefficients precede the eruptive events in comparison with the periods of high emissions rate CWT coefficients. This feature can be interpreted as a precursory increment of seismic energy which may be attributed to intrusion of fresh magma batches at shallower crustal levels (Chouet 2003; Battaglia et al. 2005). This assumption is consistent with the enhanced occurrence of tremor and long-period seismicity as reported by INETER for the same periods, and in turn reflected within the RSAM itself time series. Tremor and other low-frequency seismic signatures have been typically associated with displacements of magma and fluids through the conduit (Julian 1994; Chouet 1996; Yamamoto et al. 2002; Langer et al. 2011; Matsumoto et al. 2013). Accordingly, progressive gas exsolution accompanied by

Table 2 Illustration of different padding methods for the example time series: X_0, X_1, X_2 … X_{n-2}, X_{n-1}

Padding method	Illustration
Zero padding	… 0, 0, 0, X_0, X_1, X_2 … X_{n-2}, X_{n-1}, X_n, 0, 0, 0 …
Symmetric padding (SYM)	…X_2, X_1, X_0, X_0, X_1, X_2 … X_{n-2}, X_{n-1}, X_n, X_n, X_{n-1}, X_{n-2} …
Antisymmetric padding (ASYM)	…$-X_2$, $-X_1$, $-X_0$, X_0, X_1, X_2 … X_{n-2}, X_{n-1}, X_n, $-X_n$, $-X_{n-1}$, $-X_{n-2}$ …

transitions between sealing and opening of the upper conduit may precede the explosive events (Casadevall 1981).

The activity period comprising the gas exhalation event in April 2013 and the following eruption in June 2013 was slightly distinct in comparison with the eruptive events of December 2012 and February 2014. During the exhalation event, a significant pulse of SO_2 was freely released, suggesting that gas accumulated below the obstructed conduit was discharged without any explosive activity after the gas pressure in the conduit grew enough to remove the material that obstructed the vent. In view of the increasing seismicity that accompanied the exhalation event, it is plausible to consider that this exhalation was the result of incoming magma releasing gas at elevated pressures, combined with minor physical obstruction. A significant decrease in gas emissions below the normal background level prior to the explosions in June 2013 suggests that the obstruction of the conduit had intensified before the eruption, and the subsequent gradual increase in the emissions indicates that the obstructed vent was at least partially cleared by the eruptions.

The relatively low increase in the SO_2 flux measured during and following the explosive events suggests either that the intruded magma was already essentially degassed, or alternatively, that the clearing of the conduit was not very efficient. Although the heavy rain season during July–September may have contributed to partially seal the upper part of the conduit and a subsequent overpressure, the former option is likely more plausible since the sustained decreasing of both, SO_2 emissions and RSAM, indicates that a shallow gas accumulation is doubtful. This is further supported by the fact that the eruptions in February 2014 were again preceded by gradually increasing gas emissions, without any indication of a sustained obstruction. Further studies involving petrological evidence are required in order to better estimate the mechanisms behind the eruptive events described in this study.

Implications for volcanic surveillance

The CWT coefficient signals produced by each eruptive have similar features: at the eruption onset and during eruptive periods both time series show significant CWT coefficients with increased magnitudes shifted to higher frequencies. From previous studies where continuous SO_2 flux and RSAM measurements were made, it has correspondingly been demonstrated that by analysing the spectral signatures of their time series it is to some extent possible to identify the separate contributions of geophysical parameters such as deformation, tremor, long-period seismicity and tidal cycles (Conde et al. 2013; Bredemeyer and Hansteen 2014; Saballos et al. 2014). Moreover, the spectral contents of these time series are typically not stationary. Hence, major variations of their spectral signatures can be associated with anomalies, which in the case of San Cristóbal volcano are in good agreement with eruptive events. Thus, the ability of the XWT for detecting common spectral anomalies of SO_2 and RSAM makes this tool suitable for surveillance of volcanoes with a similar eruptive behaviour as San Cristóbal. In addition, as described in Eqs. (2)–(7), these algorithms are relatively easy to implement in a near-real-time graphical data presentation of qualitative changes in eruptive activity.

Despite the potential of this method as a volcanic activity forecasting tool, CWT and XWT have one main limitation, since the time series are finite and CWT assumes a cyclic time series, the resulting coefficients at both ends of the times series have some degree of distortion. The area where edge distortion occurs on a CWT or XWT contour map is typically termed as the cone of influence (COI), shown in Fig. 6a. This limitation may be of minor importance for studies intended to perform a post-analysis of the eruptive records. However, when considering the XWT of SO_2 emissions and RSAM as a potential tool for near-real-time volcanic monitoring, it is necessary to note that the most recent measurements are going to lie within the COI. Many different approaches have been suggested in order to reduce the distortion caused by the border effects in the COI. However, the simplest solution consists of extending the borders of the original time series by appending values (padding) before applying either the CWT or XWT, while the output of the analysis is shortened to the originals borders. The padding methods investigated in this study and illustrated in Table 2 include zero padding, extended padding, periodical padding and antisymmetric padding (Su et al. 2011; Pacola et al. 2013). In addition, it is important to underline that the area of the COI depends on the selected wavelet, because narrower wavelets result in less distorted coefficients since the area of the COI is smaller (Torrence and Compo 1998).

We examine the distortion of the COI by combining different padding methods and different wavelets. To do this,

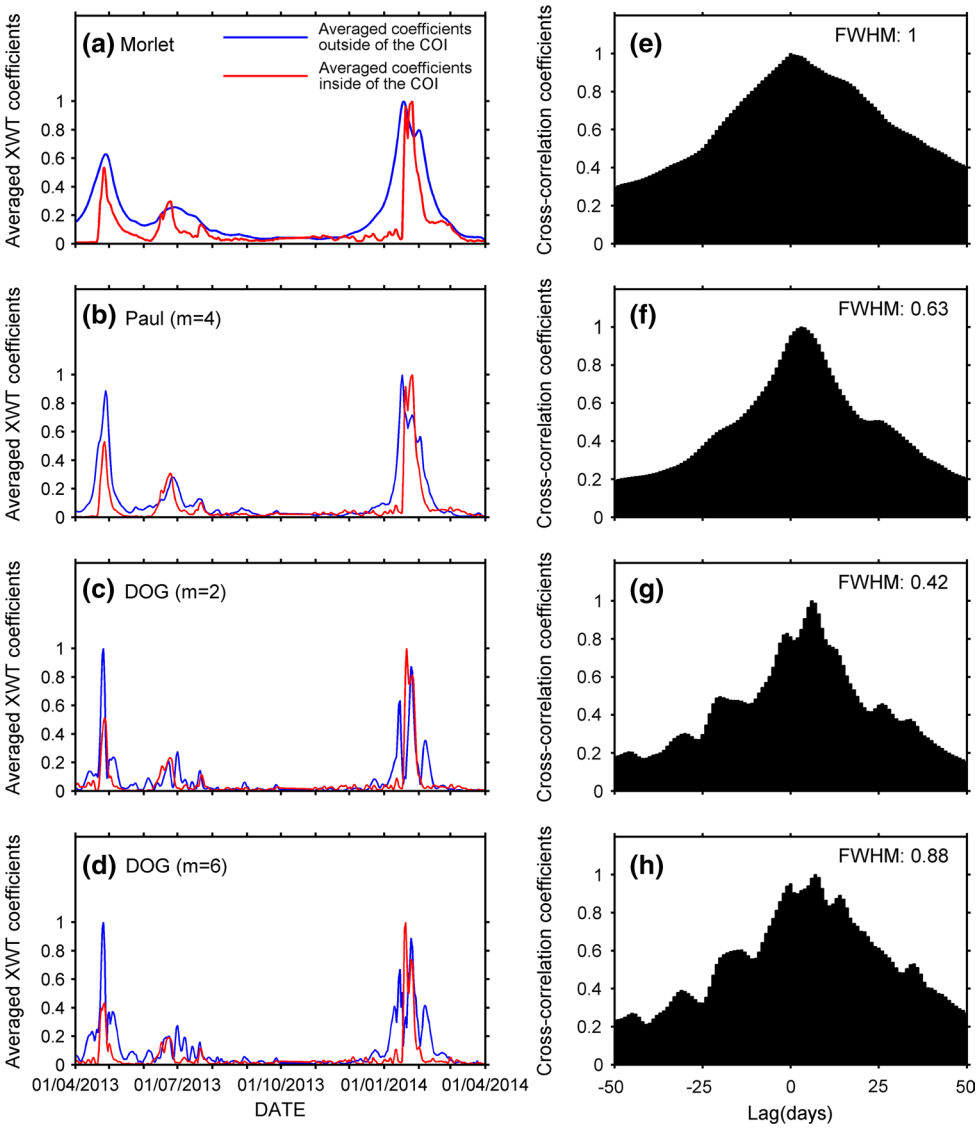

Fig. 7 Comparison of the XWT and border effects. In the *left column*, the *blue lines* correspond to the XWT scale-averaged coefficients unperturbed by the COI. The *red lines* correspond to the averaged coefficients lying in the *left* boundary of the COI. The pairs of time series in **a**–**c** were padded using antisymmetric padding (ASYM), whereas in **d** zero padding was used instead. In the *right column*, the cross-correlations between each pair of time series on the *left side* are depicted. The FWHM of the different wavelets is relative to the FWHM of the Morlet wavelet. The lower FWHMs suggest that the wavelets Paul (**f**) and DOG ($m = 2$) (**g**) are less affected by the border effect

we simulated a time series of XWT averaged coefficients derived from the SO_2-RSAM measurements, by sequentially calculating their XWT for every daily measurement within a time window containing the previous 100 measurements. The simulated time series comprises the scale-averaged XWT coefficients at the end of the current time window, which are distorted due to the border effect and represent a real-time scenario when a new measurement of SO_2 and RSAM is added to the time series. The Morlet wavelet is well suited for analysing time series over extended periods, due to its time–frequency properties. Hence, the Morlet scale-averaged XWT shown in Fig. 6b provides a good reference for comparing the performance of the simulated time series. The results of this comparison of different wavelets on the simulated time series are shown in Fig. 7a–d. After several evaluations, it was found that the antisymmetric padding produced lower errors except in the case of the wavelet DOG ($m = 6$) where zero padding was used instead. Although at first glance the distortion is obvious, the curve progression of the averaged coefficients inside the COI still resembles the qualitative variations of the averaged coefficients that are not affected by distortion. The qualitative comparisons for different wavelets are completed with the cross-correlation analysis shown in Fig. 7e–h. By observing the full width at half maximum (FWHM), we can state that out of the considered wavelets, Paul (Fig. 7e) and DOG (2) (Fig. 7f) have a lower distortion due to the COI effect, which is not surprising considering that these two wavelets are narrower. Although the Morlet wavelet coefficients are optimal for analysing time series over extended periods, the symmetry and smoothness of the correlogram shown in Fig. 7e suggest that the Paul wavelet, at least in this case, is the best option for applying averaged XWT coefficients as a qualitative forecasting tool

for a joint analysis of SO_2 emissions and RSAM in near-real time.

Conclusions

The continuous activity at San Cristóbal volcano, notable by its persistent degassing and seismicity, has allowed us to propose a novel approach for a joint analysis of SO_2 fluxes and RSAM. Initially we have described a SO_2 flux pre-processing approach implemented by using the Kalman filter which takes into account measurement errors and the estimated variability. Several studies with the aim of better constraining flux measurement errors are in progress, and this simplified statistical approach for SO_2 flux time series can be easily adapted to further improve error analysis and thus provide more accurate statistics. Furthermore, it has been shown that analysing SO_2 fluxes and RSAM by observing their CWT coefficients provides additional insights that are not so obvious at first glance. As a result, it was graphically easy to identify the increasing seismic energy preceding major eruptive events, which may be associated with magma emplacement to shallower crustal levels.

Although joint analysis of seismicity and emissions has been applied in several scenarios, the analysis presented here demonstrates the use of CWT and XWT for interpretation and surveillance of eruptive events. In the case of San Cristóbal volcano, the contours of the XWT coefficients and the peaks of the averaged coefficients correlate well with the reported eruptive events. We have also demonstrated the possibility of implementing a routine for near-real-time observations by analysing the errors and distortion due to the border effect. In this case, by using narrower wavelets such as Paul, it is possible to reduce this artefact. Although such techniques can be applied to other volcanos with continuous degassing, an extensive analysis of previous degassing and seismic reports is necessary in order to define a suitable threshold that allows to identify significant changes in the ongoing volcanic activity.

In summary, this paper demonstrates another application of using permanent DOAS instruments for continuous measurements of SO_2 in complement to the widely used seismic monitoring techniques.

Acknowledgments This work was supported by the Swedish International Development Cooperation Agency (Sida) through the International Science Program (ISP), in coordination with Instituto Nicaragüense de Estudios Territoriales (INETER). Further support was received from the Helmholtz Foundation through the "Remote Sensing and Earth System Alliance" (HA-310/IV010). We would like to thank the staff from INETER for their friendly support and in particular for the assistance and dedication provided by David Chavarría and Hoffman Sanchez. We would like to thank the reviewers and the editor of this paper for their constructive comments.

References

Allen M, Smith LA (1996) Monte Carlo SSA: detecting irregular oscillations in the presence of colored noise. J Clim 9(12):3373–3404. doi:10.1175/1520-0442(1996)009<3373:MCSDIO>2.0.CO;2

Anderson JL (2001) An ensemble adjustment kalman filter for data assimilation. Mon Weather Rev 129(12):2884–2903. doi:10.1175/1520-0493(2001)129<2884:AEAKFF>2.0.CO;2

Barrancos J, Roselló JI, Calvo D, Padrón E, Melián G, Hernández PA, Pérez NM, Millán MM, Galle B (2008) SO2 emission from active volcanoes measured simultaneously by COSPEC and mini-DOAS. Pure appl Geophys 165(1):115–133

Battaglia J, Ferrazzini V, Staudacher T, Aki K, Cheminée J-L (2005) Pre-eruptive migration of earthquakes at the Piton de la Fournaise volcano (Réunion Island). Geophys J Int 161(2):549–558. doi:10.1111/j.1365-246X.2005.02606.x

Bluth G, Shannon J, Watson I, Prata A, Realmuto V (2007) Development of an ultra-violet digital camera for volcanic SO 2 imaging. J Volcanol Geoth Res 161(1):47–56

Boichu M, Oppenheimer C, Tsanev V, Kyle PR (2010) High temporal resolution SO 2 flux measurements at Erebus volcano, Antarctica. J Volcanol Geoth Res 190(3):325–336

Bredemeyer S, Hansteen T (2014) Synchronous degassing patterns of the neighbouring volcanoes Llaima and Villarrica in south-central Chile: the influence of tidal forces. Int J Earth Sci (Geol Rundsch) 103(7):1999–2012. doi:10.1007/s00531-014-1029-2

Burton M, Allard P, Mure F, La Spina A (2007) Magmatic gas composition reveals the source depth of slug-driven Strombolian explosive activity. Science 317(5835):227–230. doi:10.1126/science.1141900

Burton MR, Caltabiano T, Murè F, Salerno G, Randazzo D (2009) SO2 flux from Stromboli during the 2007 eruption: results from the FLAME network and traverse measurements. J Volcanol Geoth Res 182(3–4):214–220. doi:10.1016/j.jvolgeores.2008.11.025

Casadevall TJ (1981) The 1980 eruptions of Mount St. Helens, Washington. SO2 emission rates at Mount St. Helens from March 29 through December 1980. US Geol Surv Prof Pap 1250:193–200

Casadevall T, Rose W, Gerlach T, Greenland LP, Ewert J, Wunderman R, Symonds R (1983) Gas emissions and the eruptions of Mount St. Helens through 1982. Science 221(4618):1383–1385

Chouet BA (1996) Long-period volcano seismicity: its source and use in eruption forecasting. Nature 380(6572):309–316

Chouet B (2003) Volcano seismology. Pure appl Geophys 160(3–4):739–788

Conde V, Bredemeyer S, Duarte E, Pacheco J, Miranda S, Galle B, Hansteen T (2013) SO2 degassing from Turrialba Volcano linked to seismic signatures during the period 2008–2012. Int J Earth Sci (Geol Rundsch). doi:10.1007/s00531-013-0958-5

Daag AS, Tubianosa BS, Newhall CG, Tungol NM, Javier D, Dolan MT, Delos Reyes PJ, Arboleda RA, Martinez MML, Regalado TM (1996) Monitoring sulfur dioxide emission at Mount Pinatubo. In: Newhall C, Punongbayan R (eds) Fire and mud: eruptions and lahars of Mount Pinatubo, Philippines, Philippine Institute of Volcanology and Seismology, Quezon city, and University of Washington Press, Seattle, pp 409–414

D'Alessandro A, Scarfì L, Scaltrito A, Di Prima S, Rapisarda S (2013) Planning the improvement of a seismic network for monitoring active volcanic areas: the experience on Mt. Etna. Adv Geosci 36:39–47

Daubechies I (1990) The wavelet transform, time-frequency localization and signal analysis. IEEE Trans Inf Theory 36(5):961–1005

De Moortel I, Ireland J, Walsh R (2000) Observation of oscillations in coronal loops. Astron Astrophys 355:L23–L26

Edmonds M, Herd RA, Galle B, Oppenheimer CM (2003) Automated, high time resolution measurements of SO2 flux at Soufrière Hills Volcano, Montserrat. Bull Volcanol 65(8):578–586

Endo ET, Murray T (1991) Real-time seismic amplitude measurement (RSAM): a volcano monitoring and prediction tool. Bull Volcanol 53(7):533–545

Evensen G (2003) The ensemble Kalman filter: theoretical formulation and practical implementation. Ocean Dyn 53(4):343–367

Fischer von Mollard K (2013) Variationen in den SO2-Ausstößen des San Cristóbal Vulkans zwischen 2006 und 2012 ermittelt anhand von bodenbasierter UV-Spektometrie (Mini-DOAS). University of Kiel, Kiel

Galle B, Oppenheimer C, Geyer A, McGonigle AJS, Edmonds M, Horrocks L (2002) A miniaturised ultraviolet spectrometer for remote sensing of SO2 fluxes: a new tool for volcano surveillance. J Volcanol Geoth Res 119(1–4):241–254

Galle B, Johansson M, Rivera C, Zhang Y, Kihlman M, Kern C, Lehmann T, Platt U, Arellano SR, Hidalgo S (2010) Network for observation of volcanic and atmospheric change (NOVAC)—a global network for volcanic gas monitoring: network layout and instrument description. J Geophys Res 115(D5):D05304. doi:10.1029/2009jd011823

Grinsted A, Moore JC, Jevrejeva S (2004) Application of the cross wavelet transform and wavelet coherence to geophysical times series. Nonlinear Process Geophys 11(5–6):561–566

Hidalgo S, Battaglia J, Arellano S, Steele A, Bernard B, Bourquin J, Galle B, Arrais S, Vásconez F (2015) SO 2 degassing at Tungurahua volcano (Ecuador) between 2007 and 2013: transition from continuous to episodic activity. J Volcanol Geoth Res 298:1–14

Hoff RM, Millan MM (1981) Remote SO2 mass flux measurements using COSPEC. J Air Pollut Control Assoc 31(4):381–384

Johansson M (2009) Application of passive DOAS for studies of megacity air pollution and volcanic gas emissions. Ph.D. thesis Chalmers University of Technology

Julian BR (1994) Volcanic tremor: nonlinear excitation by fluid flow. J Geophys Res Solid Earth 99(B6):11859–11877. doi:10.1029/93JB03129

Kalman RE (1960) A new approach to linear filtering and prediction problems. Trans ASME J Basic Eng 82(Series D):35–45. doi:10.1115/1.3662552

Kestin TS, Karoly DJ, Yano JI, Rayner NA (1998) Time-frequency variability of ENSO and stochastic simulations. J Clim 11(9):2258–2272

Langer H, Falsaperla S, Messina A, Spampinato S, Behncke B (2011) Detecting imminent eruptive activity at Mt Etna, Italy, in 2007–2008 through pattern classification of volcanic tremor data. J Volcanol Geoth Res 200(1–2):1–17. doi:10.1016/j.jvolgeores.2010.11.019

Lau K, Weng H (1995) Climate signal detection using wavelet transform: how to make a time series sing. Bull Am Meteorol Soc 76(12):2391–2402

Mather TA, Pyle DM, Tsanev VI, McGonigle AJS, Oppenheimer C, Allen AG (2006) A reassessment of current volcanic emissions from the Central American arc with specific examples from Nicaragua. J Volcanol Geoth Res 149(3–4):297–311. doi:10.1016/j.jvolgeores.2005.07.021

Matsumoto S, Shimizu H, Matsushima T, Uehira K, Yamashita Y, Nakamoto M, Miyazaki M, Chikura H (2013) Short-term spatial change in a volcanic tremor source during the 2011 Kirishima eruption. Earth Planets Space 65(4):323–329

Mori T, Burton M (2006) The SO2 camera: a simple, fast and cheap method for ground-based imaging of SO2 in volcanic plumes. Geophys Res Lett 33(24):L24804. doi:10.1029/2006GL027916

Mulquiney JE, Norton JP, Jakeman AJ, Taylor JA (1995) Random walks in the Kalman filter: implications for greenhouse gas flux deductions. Environmetrics 6(5):473–478. doi:10.1002/env.3170060509

Mwale D, Gan TY (2005) Wavelet analysis of variability, teleconnectivity, and predictability of the September–November East African rainfall. J Appl Meteorol 44(2):256–269. doi:10.1175/JAM2195.1

Myers K, Tapley BD (1976) Adaptive sequential estimation with unknown noise statistics. IEEE Trans Autom Control 21(4):520–523. doi:10.1109/TAC.1976.1101260

Nadeau PA, Palma JL, Waite GP (2011) Linking volcanic tremor, degassing, and eruption dynamics via SO2 imaging. Geophys Res Lett 38(1):L01304. doi:10.1029/2010GL045820

Nagarajan K, Judge J, Monsivais-Huertero A, Graham WD (2012) Impact of assimilating passive microwave observations on root-zone soil moisture under dynamic vegetation conditions. IEEE Trans Geosci Remote Sens 50(11 PART1):4279–4291

Olmos R, Barrancos J, Ivera CR, Barahona F, López DL, Henriquez B, Hernández A, Benitez E, Hernández PA, Pérez NM, Galle BO (2007) Anomalous emissions of SO2 during the recent eruption of Santa Ana volcano, El Salvador, Central America. Pure Appl Geophys 164(12):2489–2506

Pacola ER, Quandt VI, Schneider FK, Sovierzoski MA (2013) The wavelet transform border effect in EEG spike signals. In: Long M (ed) IFMBE proceedings of the world congress on medical physics and biomedical engineering, May 26–31, 2012, Beijing, China, vol 39. Springer, Berlin, pp 593–596. doi:10.1007/978-3-642-29305-4_155

Petersen T, Caplan-Auerbach J, McNutt SR (2006) Sustained long-period seismicity at Shishaldin Volcano, Alaska. J Volcanol Geoth Res 151(4):365–381

Platt U, Stutz J (2008) Differential optical absorption spectroscopy (DOAS), principle and applications. Springer, Heidelberg. doi:10.1007/978-3-540-75776-4

Rivera C (2009) Application of passive DOAS using scattered sunlight for quantification of gas emissions from anthropogenic and volcanic sources. Chalmers tekniska högskola, Gothenburg

Rivera C, Garcia JA, Galle B, Alonso L, Yan Z, Johansson M, Matabuena M, Gangoiti G (2009) Validation of optical remote sensing measurement strategies applied to industrial gas emissions. Int J Remote Sens 30(12):3191–3204. doi:10.1080/01431160802558808

Saballos J, Conde V, Malservisi R, Connor C, Álvarez J, Muñoz A (2014) Relatively short-term correlation among deformation, degassing, and seismicity: a case study from Concepción volcano, Nicaragua. Bull Volcanol 76(8):1–11. doi:10.1007/s00445-014-0843-5

Smithsonian-Institution (2014) http://www.volcano.si.edu/volcano.cfm?vn=344020

Su H, Liu Q, Li J (2011) Alleviating border effects in wavelet transforms for nonlinear time-varying signal analysis. Adv Electr Comput Eng 11(3):55–60

Symonds R, Rose WI, Bluth GJS, Gerlach TM (1994) Volcanic-gas studies; methods, results, and applications. Rev Mineral Geochem 30(1):1–66

Tilling RI (2008) The critical role of volcano monitoring in risk reduction. Adv Geosci 14:3–11

Torrence C, Compo GP (1998) A practical guide to wavelet analysis. Bull Am Meteorol Soc 79(1):61–78. doi:10.1175/1520-0477(1998)079<0061:APGTWA>2.0.CO;2

Torrence C, Webster PJ (1999) Interdecadal changes in the ENSO—monsoon system. J Clim 12(8):2679–2690. doi:10.1175/1520-0442(1999)012<2679:ICITEM>2.0.CO;2

Waite GP, Nadeau PA, Lyons JJ (2013) Variability in eruption style and associated very long period events at Fuego volcano, Guatemala. J Geophys Res Solid Earth 118(4):1526–1533

Wang P, Gao J (2013) Extraction of instantaneous frequency from seismic data via the generalized Morse wavelets. J Appl Geophys 93:83–92

Welch G, Bishop G (1995) An introduction to the Kalman filter. University of North Carolina, Chapel Hill

Weng H, Lau K (1994) Wavelets, period doubling, and time-frequency localization with application to organization of convection over the tropical western Pacific. J Atmos Sci 51(17):2523–2541

Yamamoto M, Kawakatsu H, Yomogida K, Koyama J (2002) Long-period (12 sec) volcanic tremor observed at Usu 2000 eruption: seismological detection of a deep magma plumbing system. Geophys Res Lett 29(9):43-1–43-4

Yan Y, Barth A, Beckers JM (2014) Comparison of different assimilation schemes in a sequential Kalman filter assimilation system. Ocean Model 73:123–137